

Physics-Constrained Learning of Energy-Preserving Stencils for Maxwell’s Equations

Victory C. Obieke

Department of Mathematics, Oregon State University
 obiekev@oregonstate.edu

Abstract

We study data-driven construction of spatial discretizations for the one-dimensional Maxwell system. Using high-fidelity training data from a spectral discretization, we learn a *linear convolution stencil* that approximates the spatial derivative operator in Maxwell’s equations. We formulate a convex quadratic program for the stencil coefficients with linear constraints that enforce skew-adjointness of the discrete derivative; these constraints guarantee a semi-discrete electromagnetic energy identity and yield a CFL condition expressed directly in terms of the stencil’s Fourier symbol. We compare several convex solvers for the resulting quadratic program—projected gradient, Nesterov-accelerated gradient, ADMM, and an interior-point reference implemented in CVXPY—and evaluate the learned operators in time-dependent Maxwell simulations using a Crank–Nicolson (CN) discretization. Numerical experiments, including cases with nonstandard target operators and noisy training data, show that (i) energy-constrained learned stencils achieve accuracy comparable to standard central differences while exactly preserving the discrete electromagnetic energy under CN time-stepping, and (ii) ADMM and interior-point solvers produce nearly identical operators, with ADMM offering a favorable tradeoff between accuracy, constraint satisfaction, and runtime.

1 Introduction

Finite-difference time-domain (FDTD) methods are a standard tool for solving Maxwell’s equations in computational electromagnetics [21]. Classical schemes, such as the Yee method, are derived by hand from the continuous equations, with spatial derivatives approximated using fixed central-difference stencils and stability enforced via analytical CFL conditions. Recently, there has been growing interest in *data-driven discretizations*, where discrete operators are learned from numerical or experimental data, for example via regression or neural networks. Examples include data-driven discretization of Burgers and Navier–Stokes equations and learned coarse-grid operators for PDEs [1].

Most existing data-driven schemes aim to minimize approximation error but do not explicitly enforce structural properties such as stability, conservation, or energy balance. For Maxwell’s equations this is a significant limitation, since standard FDTD schemes are carefully designed so that discrete versions of divergence constraints and energy identities hold at the semi-discrete level.

In this work we address this gap in a simple but concrete setting: the one-dimensional Maxwell system with periodic boundary conditions. Our goal is to learn a discrete spatial derivative operator

$$D : \mathbb{R}^N \rightarrow \mathbb{R}^N$$

represented as a convolution stencil, directly from data. We impose linear constraints on the stencil that enforce *skew-adjointness* of D with respect to the discrete L^2 inner product. This structural

constraint guarantees exact conservation of discrete electromagnetic energy at the semi-discrete level, regardless of the details of the training data.

Classical FDTD schemes such as the Yee method [21] are hand-derived so that the discrete curl operator is skew-adjoint, yielding exact semi-discrete energy conservation. High-order extensions and operator-splitting schemes similarly maintain this structure [3, 6].

Data-driven PDE schemes learn local stencils or coarse-grid operators directly from numerical data. Bar-Sinai et al. learn finite-difference discretizations for Burgers and Navier–Stokes, showing that learned operators can match or exceed classical schemes on specific training distributions [1]. Many follow-up works learn PDE operators or closure models [17, 11, 20, 18, 9], but typically do not enforce stability, skew-adjointness, or conservation laws.

Recent neural-operator surrogates for electromagnetics incorporate physics through architectural biases or penalty terms. Dynamic-convolution neural operators for FDTD-like EM propagation impose causal receptive fields and material dispersion structure [14]. Domain-decomposition neural operators couple learned subdomain solvers through interface penalties or consistency conditions [15, 8]. Other neural operator frameworks embed conservation via soft constraints or corrective layers [13, 12]. These approaches improve stability but enforce physical structure only approximately, through optimization.

Building on this context, our main contributions are as follows. First, we formulate a convex quadratic optimization problem for learning convolution stencils for the 1D Maxwell system from spectral training data, with an objective given by a least-squares misfit between the learned discrete derivative and high-fidelity derivatives, and linear constraints that encode skew-symmetry of the stencil coefficients together with simple box bounds. Second, we show that these linear constraints are *exactly* equivalent to skew-adjointness of the corresponding convolution operator with respect to the discrete L^2 inner product, and hence to a semi-discrete electromagnetic energy identity, yielding what is, to our knowledge, the first learned Maxwell stencil with a *guaranteed* semi-discrete energy conservation law. Third, we characterize the numerical wave speed and associated CFL restriction of the learned discrete curl operator purely in terms of its Fourier symbol $\mu(\theta)$. Finally, we implement projected gradient, Nesterov-accelerated gradient, ADMM, and an interior-point method (via CVXPY) to solve the constrained quadratic program, and we benchmark the resulting stencils in time-dependent 1D Maxwell simulations; the experiments compare PDE error, energy-constraint residuals, and energy evolution across stencil radii, and demonstrate that ADMM and interior-point methods produce nearly identical, highly accurate stencils, with ADMM offering a favorable tradeoff between accuracy, constraint satisfaction, and runtime.

Although our experiments focus on a simple 1D periodic model, the framework and energy constraints extend naturally to higher-dimensional settings and more complex material models. Our results illustrate how even simple linear constraints in a data-driven discretization can encode important physics and restore structural properties such as energy conservation.

Our method imposes *hard* linear constraints that make the learned convolution stencil exactly skew-adjoint, guaranteeing a discrete electromagnetic energy identity independent of training accuracy or solver choice. This places our work closest to Bar-Sinai et al. but with strict structure preservation rather than penalty-based regularization, and complementary to physics-informed neural operators, which typically enforce conservation approximately. To the best of our knowledge, this is the first work to combine data-driven stencil learning for Maxwell’s equations with linear constraints that (i) exactly characterize skew-symmetric convolution operators and (ii) yield a rigorous semi-discrete energy identity and a CFL condition expressed directly in terms of the learned stencil’s Fourier symbol. This provides a bridge between unconstrained data-driven discretizations and classical energy-preserving FDTD schemes, while remaining compatible with standard convex optimization toolchains (projected gradient, Nesterov acceleration, ADMM, and interior-point

solvers).

Beyond the homogeneous model, Sections 6.6 and 6.7 illustrate how the same constrained learning framework can recover nonstandard, effective operators and regularize noisy or mildly inconsistent training data.

2 Semi-discrete Maxwell system and energy identity

We consider the 1D Maxwell system in vacuum, written in non-dimensional form with $\varepsilon_0 = \mu_0 = 1$:

$$\partial_t E = \partial_x H, \quad \partial_t H = \partial_x E, \quad (1)$$

on the periodic domain $[0, L]$.

We discretize space using a uniform grid $x_i = i\Delta x$, $i = 0, \dots, N-1$, with $\Delta x = L/N$, and collect the nodal values of the electric and magnetic fields into vectors

$$\mathbf{E}(t) = (E_0(t), \dots, E_{N-1}(t))^\top, \quad \mathbf{H}(t) = (H_0(t), \dots, H_{N-1}(t))^\top.$$

Let $D : \mathbb{R}^N \rightarrow \mathbb{R}^N$ denote a linear discrete derivative operator. In this work, D is a *convolution operator* defined by a stencil $w \in \mathbb{R}^{2R+1}$,

$$(D\mathbf{u})_i = \sum_{\ell=-R}^R w_\ell u_{i+\ell}, \quad i = 0, \dots, N-1, \quad (2)$$

with periodic wrap-around in the index $i + \ell$. The semi-discrete Maxwell system then reads

$$\frac{d}{dt}\mathbf{E}(t) = D\mathbf{H}(t), \quad \frac{d}{dt}\mathbf{H}(t) = D\mathbf{E}(t). \quad (3)$$

We equip \mathbb{R}^N with the standard discrete L^2 inner product

$$\langle \mathbf{u}, \mathbf{v} \rangle := \Delta x \sum_{i=0}^{N-1} u_i v_i, \quad \|\mathbf{u}\|^2 := \langle \mathbf{u}, \mathbf{u} \rangle. \quad (4)$$

The corresponding discrete electromagnetic energy is

$$\mathcal{E}(t) := \frac{1}{2}\|\mathbf{E}(t)\|^2 + \frac{1}{2}\|\mathbf{H}(t)\|^2. \quad (5)$$

Theorem 1 (Semi-discrete energy identity). *Let D be any linear operator on \mathbb{R}^N , and let $\mathbf{E}(t), \mathbf{H}(t)$ satisfy (3). Then*

$$\frac{d}{dt}\mathcal{E}(t) = \langle D\mathbf{H}(t), \mathbf{E}(t) \rangle + \langle D\mathbf{E}(t), \mathbf{H}(t) \rangle. \quad (6)$$

In particular, if D is skew-adjoint with respect to (4), i.e.,

$$\langle D\mathbf{u}, \mathbf{v} \rangle = -\langle \mathbf{u}, D\mathbf{v} \rangle \quad \forall \mathbf{u}, \mathbf{v}, \quad (7)$$

then the discrete energy is exactly conserved:

$$\frac{d}{dt}\mathcal{E}(t) = 0. \quad (8)$$

Proof. Differentiating (5) in time and using (3) gives

$$\begin{aligned}\frac{d}{dt}\mathcal{E}(t) &= \left\langle \frac{d}{dt}\mathbf{E}(t), \mathbf{E}(t) \right\rangle + \left\langle \frac{d}{dt}\mathbf{H}(t), \mathbf{H}(t) \right\rangle \\ &= \langle D\mathbf{H}(t), \mathbf{E}(t) \rangle + \langle D\mathbf{E}(t), \mathbf{H}(t) \rangle,\end{aligned}$$

which is (6). If D is skew-adjoint, then

$$\langle D\mathbf{H}, \mathbf{E} \rangle = -\langle \mathbf{H}, D\mathbf{E} \rangle = -\langle D\mathbf{E}, \mathbf{H} \rangle,$$

so the two terms in (6) cancel and $\frac{d}{dt}\mathcal{E}(t) = 0$. \square

2.1 Skew-symmetric convolution operators and stencil constraints

We now specialize to convolution operators of the form (2) with periodic boundary conditions. Let $w = (w_{-R}, \dots, w_{-1}, w_0, w_1, \dots, w_R)^\top$ be the stencil.

Lemma 1. *Let D be defined by (2) with periodic wrap-around. Then the matrix entries of D satisfy*

$$D_{ij} = w_{i-j}, \quad i, j = 0, \dots, N-1, \quad (9)$$

where the difference $i - j$ is taken modulo N .

Proof. By definition,

$$(D\mathbf{u})_i = \sum_{\ell=-R}^R w_\ell u_{i+\ell} = \sum_{j=0}^{N-1} w_{i-j} u_j,$$

where $j = i + \ell$ (modulo N). Hence $D_{ij} = w_{i-j}$. \square

Theorem 2 (Characterization of skew-symmetric stencils). *[3] Let D be the convolution operator (2) with periodic boundary conditions and stencil $w \in \mathbb{R}^{2R+1}$. Then D is skew-adjoint with respect to (4), i.e., $D^\top = -D$, if and only if the stencil satisfies*

$$w_0 = 0, \quad w_{-\ell} = -w_{+\ell}, \quad \ell = 1, \dots, R. \quad (10)$$

Proof. By Lemma 1 the entries of D are $D_{ij} = w_{i-j}$, so

$$(D^\top)_{ij} = D_{ji} = w_{j-i}.$$

The condition $D^\top = -D$ is therefore equivalent to

$$w_{j-i} = -w_{i-j} \quad \text{for all } i, j,$$

or, writing $\ell = i - j$,

$$w_{-\ell} = -w_{+\ell} \quad \text{for all } \ell.$$

In particular, taking $\ell = 0$ yields $w_0 = -w_0$, hence $w_0 = 0$, and for $\ell = 1, \dots, R$ we obtain $w_{-\ell} = -w_{+\ell}$. Conversely, if (10) holds, then the above computation shows $D^\top = -D$, i.e., D is skew-adjoint. \square

We encode the conditions (10) as a set of linear constraints on the stencil vector w . Let $C \in \mathbb{R}^{(R+1) \times (2R+1)}$ be defined by

$$(Cw)_0 = w_0, \quad (Cw)_\ell = w_{-\ell} + w_{+\ell}, \quad \ell = 1, \dots, R,$$

and let $d \in \mathbb{R}^{R+1}$ be the zero vector. Then the constraint $Cw = d$ is simply

$$w_0 = 0, \quad w_{-\ell} + w_{+\ell} = 0, \quad \ell = 1, \dots, R, \quad (11)$$

which is equivalent to skew-symmetry.

Corollary 1. *Let C and d be defined in (11). Then $Cw = d$ if and only if the stencil w satisfies (10), i.e., if and only if the corresponding convolution operator D is skew-adjoint.*

Proof. Immediate from (11) and Theorem 2. □

Corollary 1 shows that the linear constraint $Cw = d$ used in our optimization problem is *exactly* the condition required for semi-discrete energy conservation via Theorem 1.

3 Wave speed and CFL for the learned operator

The discrete curl operator D constructed in Section 2.1 is a periodic convolution with stencil $w = (w_{-R}, \dots, w_0, \dots, w_R)$ satisfying the skew-symmetry constraints of Theorem 2. For such an operator it is convenient to work with its Fourier symbol

$$\mu(\theta) := \sum_{k=-R}^R w_k e^{ik\theta}, \quad \theta \in [-\pi, \pi], \quad (12)$$

which characterizes the response of D to discrete Fourier modes $e^{ij\theta}$.

For the semi-discrete Maxwell system

$$\frac{d}{dt} \begin{bmatrix} \mathbf{H} \\ \mathbf{E} \end{bmatrix} = A \begin{bmatrix} \mathbf{H} \\ \mathbf{E} \end{bmatrix}, \quad A = \begin{bmatrix} 0 & D \\ D^T & 0 \end{bmatrix},$$

the eigenvalues of A are purely imaginary and can be written as $\lambda(\theta) = \pm i|\mu(\theta)|$ for $\theta \in [-\pi, \pi]$. In particular, the quantity $|\mu(\theta)|$ plays the role of a *numerical wave speed* for the mode θ , and the maximal value

$$c_{\max} := \max_{\theta \in [-\pi, \pi]} |\mu(\theta)| \quad (13)$$

is the largest speed supported by the learned operator. For the standard centered difference stencil of width three one recovers $c_{\max} \sim h^{-1}$, corresponding to the usual CFL restriction for explicit wave propagation schemes.

If one were to apply the classical leapfrog scheme to the semi-discrete system, stability of the scalar test equation $\dot{u} = \lambda u$ with $\lambda = i\omega$ requires $\Delta t |\omega| \leq 2$, see, e.g., [19, 16, 10]. Substituting $\omega = \pm|\mu(\theta)|$ and maximizing over θ yields the CFL condition

$$\Delta t \leq \frac{2}{c_{\max}}, \quad (14)$$

which expresses the admissible time step solely in terms of the learned symbol (12). In this way the learned stencil can be interpreted within the familiar CFL framework for explicit FDTD schemes, although in our numerical experiments we will use an implicit time integrator. In this work we focus on CN, which is unconditionally stable for the skew-adjoint semi-discrete operator. A systematic comparison with leapfrog using the derived CFL bound is left for future work

3.1 Crank–Nicolson time integration

For the actual time-dependent simulations in Section 6 we use the Crank–Nicolson (CN) method applied to the semi-discrete system

$$\frac{d\mathbf{U}}{dt} = A\mathbf{U}, \quad \mathbf{U} = \begin{bmatrix} \mathbf{H} \\ \mathbf{E} \end{bmatrix}, \quad A^T = -A.$$

The CN update reads

$$\frac{\mathbf{U}^{n+1} - \mathbf{U}^n}{\Delta t} = A \frac{\mathbf{U}^{n+1} + \mathbf{U}^n}{2}, \quad (15)$$

which coincides with the implicit midpoint rule for linear systems. Since A is skew-adjoint, the discrete energy

$$\mathcal{E}^n := \frac{1}{2} \|\mathbf{U}^n\|_2^2 = \frac{1}{2} (\|\mathbf{H}^n\|_2^2 + \|\mathbf{E}^n\|_2^2)$$

is preserved exactly by (15) for any time step $\Delta t > 0$; see, e.g., [6, 7] for background on such structure-preserving schemes.

In particular, CN does not require the CFL restriction (14) for stability or energy conservation in this linear, skew-adjoint setting. In the numerical experiments we nevertheless choose a time step Δt proportional to the grid spacing h and small enough that (14) would be satisfied for the corresponding centered-difference operator. This ensures that temporal discretization errors remain small relative to the spatial error while allowing us to interpret the learned stencil in terms of an effective wave speed c_{\max} .

4 Data-driven stencil learning

We now formulate the quadratic optimization problem used to learn stencils from data generated by a high-fidelity discretization.

4.1 Training data from spectral 1D Maxwell

We generate training data by sampling random Maxwell states and computing their time derivatives exactly (up to spectral discretization error). We work on the periodic domain $[0, L]$ with N grid points and spacing $\Delta x = L/N$. For each training sample we draw a random truncated Fourier series

$$\begin{aligned} E(x) &= \sum_{m=1}^{m_{\max}} a_m \sin\left(\frac{2\pi m x}{L} + \phi_m\right), \\ H(x) &= \sum_{m=1}^{m_{\max}} b_m \sin\left(\frac{2\pi m x}{L} + \psi_m\right), \end{aligned}$$

with amplitudes a_m, b_m and phases ϕ_m, ψ_m drawn from simple Gaussian and uniform distributions. We then compute the spatial derivatives $\partial_x E$ and $\partial_x H$ spectrally using FFTs:

$$\partial_x E = \mathcal{F}^{-1}\left(\mathrm{i}k \hat{E}\right), \quad \partial_x H = \mathcal{F}^{-1}\left(\mathrm{i}k \hat{H}\right),$$

where k is the discrete wavenumber. Finally, we obtain the time derivatives from the PDE (1):

$$\partial_t E = \partial_x H, \quad \partial_t H = \partial_x E.$$

We denote by

$$U \in \mathbb{R}^{n_{\text{sims}} \times 2 \times N}$$

the array of training states, where $U[s, 0, i] = E^{(s)}(x_i)$ and $U[s, 1, i] = H^{(s)}(x_i)$ denote the electric and magnetic fields of the s -th training sample evaluated at the grid point x_i . Similarly,

$$\frac{dU}{dt} \in \mathbb{R}^{n_{\text{sims}} \times 2 \times N}$$

stores the corresponding time derivatives, with $(dU/dt)[s, 0, i] = \partial_t E^{(s)}(x_i)$ and $(dU/dt)[s, 1, i] = \partial_t H^{(s)}(x_i)$.

Here n_{sims} denotes the number of independent training samples (or snapshots), each consisting of a randomly generated Maxwell state (E, H) and its corresponding time derivative. The spatial domain $[0, L]$ is discretized using N uniformly spaced grid points $x_i = i\Delta x$, $i = 0, \dots, N-1$, where $\Delta x = L/N$.

4.2 Least-squares formulation

Given training pairs (\mathbf{E}, \mathbf{H}) and $(\partial_t \mathbf{E}, \partial_t \mathbf{H})$, we wish to learn a single convolution stencil w such that

$$D\mathbf{H} \approx \partial_x \mathbf{H} = \partial_t \mathbf{E}, \quad D\mathbf{E} \approx \partial_x \mathbf{E} = \partial_t \mathbf{H},$$

in a least-squares sense. Because we assume periodic boundary conditions, the stencil is applied identically at every grid point, with indices interpreted modulo N .

For each grid index i we extract local patches

$$\mathbf{h}_i = (H_{i-R}, \dots, H_{i+R})^\top, \quad \mathbf{e}_i = (E_{i-R}, \dots, E_{i+R})^\top,$$

and define scalar targets

$$y_i^{(H)} = \partial_t E_i, \quad y_i^{(E)} = \partial_t H_i.$$

The desired relationships are

$$w^\top \mathbf{h}_i \approx y_i^{(H)}, \quad w^\top \mathbf{e}_i \approx y_i^{(E)}.$$

Stacking all patches and targets over space and all simulations, we obtain a linear system

$$Aw \approx b, \tag{16}$$

where each row of A is either \mathbf{h}_i^\top or \mathbf{e}_i^\top , and b collects the corresponding targets. This leads to the unconstrained least-squares problem

$$\min_{w \in \mathbb{R}^{2R+1}} \frac{1}{2} \|Aw - b\|_2^2 + \frac{\lambda}{2} \|w\|_2^2, \tag{17}$$

where $\lambda \geq 0$ is a small Tikhonov regularization parameter.

4.3 Energy constraint and box bounds

To enforce skew-adjointness and hence discrete energy conservation, we impose the linear constraint $Cw = d$ with C and d defined as in Section 2.1. By Corollary 1, any stencil satisfying $Cw = d$ defines a skew-adjoint convolution operator D and therefore an energy-conserving semi-discrete Maxwell system.

We also impose simple box bounds $|w_\ell| \leq M$, i.e.,

$$-M \leq w_\ell \leq M, \quad \ell = -R, \dots, R, \quad (18)$$

where $M > 0$ is chosen large enough to contain the true derivative stencil but small enough to control numerical conditioning.

Our final optimization problem is the convex quadratic program

$$\begin{aligned} \min_{w \in \mathbb{R}^{2R+1}} \quad & \frac{1}{2} \|Aw - b\|_2^2 + \frac{\lambda}{2} \|w\|_2^2, \\ \text{s.t.} \quad & Cw = d, \\ & -M \leq w \leq M. \end{aligned} \quad (19)$$

This problem is strictly convex for $\lambda > 0$ and admits a unique solution. For our first-order methods we use a slightly simplified variant of (19) in which only the linear energy constraint is enforced. Specifically, projected gradient (PG) and Nesterov-accelerated gradient (NAG) are applied to the equality-constrained problem

$$\begin{aligned} \min_{w \in \mathbb{R}^{2R+1}} \quad & \frac{1}{2} \|Aw - b\|_2^2 + \frac{\lambda}{2} \|w\|_2^2, \\ \text{s.t.} \quad & Cw = d, \end{aligned} \quad (20)$$

while the full equality-plus-box-constrained problem (19) is handled by ADMM and the interior-point solver in CVXPY. In our experiments the solutions of (20) produced by PG and NAG remain well inside the box $[-M, M]^{2R+1}$, so the difference between (20) and (19) is negligible in practice. In the presence of noisy or mildly inconsistent training data, the least-squares system can become ill-conditioned and produce stencils with very large coefficients; the Tikhonov term and box bounds mitigate this behavior, as illustrated in Section 6.7.

5 Convex solvers

We briefly summarize the algorithms used to solve (19). All methods operate on the same design matrix A , constraint matrix C , and bounds.

5.1 Projected gradient methods

Our first two solvers are projected gradient (PG) and Nesterov-accelerated gradient (NAG), applied to the *equality-constrained* problem (20). In particular, for PG/NAG we enforce only the linear energy constraint $Cw = d$ and do not explicitly impose the box bounds $-M \leq w \leq M$. In our experiments the PG/NAG iterates remain strictly inside the box, so the resulting solutions agree (to numerical tolerance) with those of the fully constrained problem (19).

Define the feasible affine subspace

$$\mathcal{C}_{\text{eq}} = \{w \in \mathbb{R}^{2R+1} : Cw = d\}.$$

The orthogonal projection onto \mathcal{C}_{eq} with respect to the Euclidean inner product is given explicitly by

$$P_{\mathcal{C}_{\text{eq}}}(z) := z - C^\top(CC^\top)^{-1}(Cz - d), \quad z \in \mathbb{R}^{2R+1}, \quad (21)$$

assuming that C has full row rank.

Let

$$f(w) := \frac{1}{2}\|Aw - b\|_2^2 + \frac{\lambda}{2}\|w\|_2^2, \quad \nabla f(w) = A^\top(Aw - b) + \lambda w.$$

We choose a stepsize $\alpha = 1/L$, where one may take $L = \|A\|_2^2 + \lambda = \|A^\top A\|_2 + \lambda$.

For PG, the update is

$$w^{k+1} = P_{\mathcal{C}_{\text{eq}}}\left(w^k - \alpha \nabla f(w^k)\right),$$

with $P_{\mathcal{C}_{\text{eq}}}$ given by (21).

For NAG we use the extrapolated point

$$y^k = w^k + \beta_k(w^k - w^{k-1}),$$

and then update

$$w^{k+1} = P_{\mathcal{C}_{\text{eq}}}\left(y^k - \alpha \nabla f(y^k)\right),$$

with the standard parameters

$$t_{k+1} = \frac{1}{2}\left(1 + \sqrt{1 + 4t_k^2}\right), \quad \beta_k = \frac{t_k - 1}{t_{k+1}}, \quad t_0 = 1.$$

We track the objective $f(w^k)$, wall-clock time, and the equality residual $\|Cw^k - d\|_2$ at each iteration.

Remark 1. *Projecting sequentially onto $\{Cw = d\}$ and the box $[-M, M]^{2R+1}$ is not, in general, the exact Euclidean projection onto their intersection. If the box constraint becomes active and one wishes to enforce both constraints within a projected-gradient framework, one should compute $P_{\{Cw=d\} \cap [-M, M]^{2R+1}}$ using an intersection projection method such as Dykstra's algorithm, or solve the projection step as a small quadratic program.*

5.2 ADMM

To better handle the combination of equality and box constraints, we also implement an alternating direction method of multipliers (ADMM) [4], [5] scheme. We introduce a copy z of w and enforce the box constraint on z only:

$$w \in \mathbb{R}^{2R+1}, \quad z \in [-M, M]^{2R+1}, \quad w = z, \quad Cw = d.$$

The augmented Lagrangian splits into a quadratic w -problem with equality constraints and a simple proximal z -update given by box projection. The w -update reduces to solving a KKT system of the form

$$\begin{bmatrix} A^\top A + (\lambda + \rho)I & C^\top \\ C & 0 \end{bmatrix} \begin{bmatrix} w \\ \eta \end{bmatrix} = \begin{bmatrix} A^\top b + \rho(z - u) \\ d \end{bmatrix},$$

where $\rho > 0$ is the ADMM penalty parameter and η is a vector of Lagrange multipliers for the equality constraints. The z -update is just componentwise clipping, $z^{k+1} = \Pi_{[-M, M]^{2R+1}}(w^{k+1} + u^k)$, and the dual update is $u^{k+1} = u^k + (w^{k+1} - z^{k+1})$. We again monitor the objective, equality residual, and primal difference $\|w^{k+1} - w^k\|$.

5.3 Interior-point reference (CVXPY)

Finally, we use the CVXPY modeling framework with a cone solver (SCS in our experiments) to obtain a reference solution to (19). This interior-point-based solution serves as a baseline for the quality of the first-order methods. The corresponding routine `solve_cvx` sets up the quadratic objective and linear constraints, and returns the optimal stencil w_{cvx} when CVXPY is available.

6 Numerical experiments

All experiments were implemented in Python using NumPy for linear algebra and SciPy for FFTs. The ADMM and projected-gradient/Nesterov solvers are written explicitly as described in Section 5. The interior-point reference solution is computed using CVXPY (version X.Y) with the SCS solver. Runtimes are reported for a single-threaded run on a (Apple M4, 16 GB RAM) using Python 3.11. Although absolute times depend on hardware and implementation details, the relative trends between first-order methods (PG/NAG) and the second-order ADMM/CVX approach remained consistent across several runs.

We now present numerical experiments in the 1D Maxwell setting to evaluate the learned stencils and the performance of the different solvers. All experiments use the Crank–Nicolson (CN) time integrator with the learned spatial operator.

6.1 Experimental setup

Unless otherwise stated, we use the following default parameters:

- Spatial domain $[0, L]$ with $L = 1$ and $N = 64$ cells, $\Delta x = L/N$.
- Training data: $n_{\text{sims}} = 200$ random spectral samples with $m_{\text{max}} = 5$ Fourier modes.
- Regularization parameter $\lambda = 10^{-6}$ and box parameter $M = 100$.
- Stencil radii $R \in \{1, 2, 3, 4\}$, corresponding to stencil length $2R + 1$.
- Time integration: Crank–Nicolson (CN) applied to the semi-discrete system with time step $\Delta t = 0.5\Delta x$ and $N_t = 300$ time steps.

The initial condition for time integration is chosen as a single Fourier mode,

$$E(x, 0) = \sin(2\pi x/L), \quad H(x, 0) = \cos(2\pi x/L),$$

and we compute a reference solution using the exact central-difference stencil

$$w_{\text{exact}} = \frac{1}{2\Delta x}(-1, 0, 1), \tag{22}$$

We then integrate the Maxwell system with each learned stencil using CN and measure the relative L^2 error in the electric field at final time:

$$\text{err}(w) = \frac{\|\mathbf{E}^{\text{learned}}(T) - \mathbf{E}^{\text{FD}}(T)\|_2}{\|\mathbf{E}^{\text{FD}}(T)\|_2}. \tag{23}$$

We also compute the energy-constraint residual

$$r_{\text{eq}}(w) = \|Cw - d\|_2,$$

which is zero for an exactly skew-symmetric stencil.

As an additional diagnostic, we track the discrete electromagnetic energy

$$\mathcal{E}^n := \frac{1}{2}\Delta x \sum_i [(E_i^n)^2 + (H_i^n)^2]$$

over time. For the exact stencil and CN time-stepping, the code confirms that \mathcal{E}^n is constant to within floating-point roundoff, consistent with the analysis in Section 2.

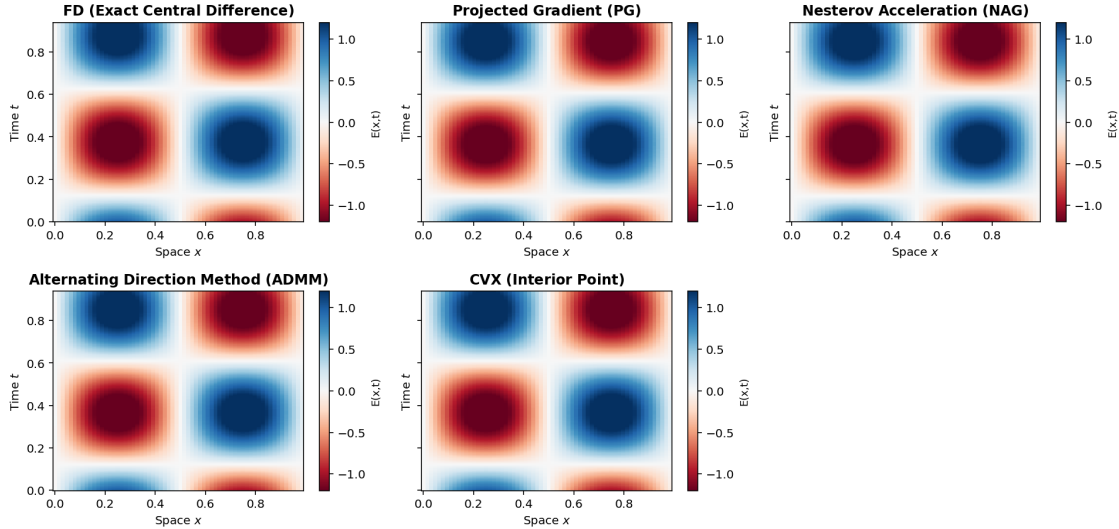


Figure 1: Space-Time Evolution

6.2 Learned stencils for $R = 1$

Table 1 shows the learned stencils obtained by each solver compared with w_{exact} . We observe that all methods recover a stencil very close to the exact one, with small differences due to the finite training set and regularization.

Method	w_{-1}	w_0	w_{+1}
Exact FD	-32.000000	0.000000	32.000000
PG	-32.906110	0.000000	32.906110
NAG	-32.906098	0.000000	32.906098
ADMM	-32.906114	-2.64×10^{-16}	32.906114
CVX	-32.906115	-1.57×10^{-14}	32.906115

Table 1: Learned stencils for radius $R = 1$.

In In Figures 1 and 2, we compare the space-time evolution and the final-time profile of the electric field $E(x, t)$ for each learned stencil against the reference FD solution for $R = 1$. The final-time and space-time profiles in Figure 2 are visually indistinguishable from the reference solution.

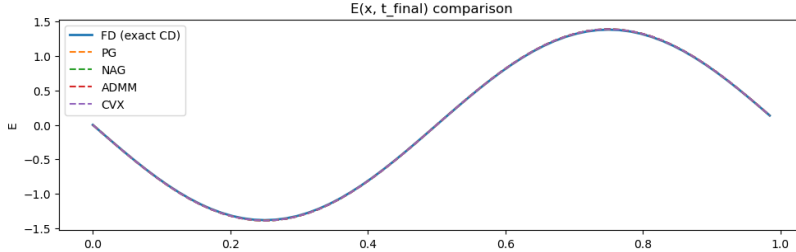


Figure 2: Final-time electric field $E(x, T)$ for the exact central-difference stencil and the learned stencils for $R = 1$ under Crank–Nicolson time-stepping. The curves are visually indistinguishable at the scale shown.

This experiment serves as a sanity check for the learning framework: for the smallest radius $R = 1$, the energy-constrained optimization recovers a stencil that is essentially indistinguishable from the classical centered difference, and the corresponding Crank–Nicolson time integration reproduces the reference solution to within plotting accuracy. In other words, when the true operator is known and low order, the learned discretizations do not degrade either accuracy or energy behavior, while providing the same skew-adjoint structure that underpins exact discrete energy conservation. This $R = 1$ case therefore provides a baseline for the higher-radius stencils and noisy-training experiments considered below.

6.3 Error and energy residual versus stencil radius

To explore the effect of stencil size, we repeat the learning and time-integration procedure for radii $R = 1, 2, 3, 4$. Figure 3 shows the final-time relative L^2 error $\text{err}(w)$ for each method as a function of R . We initialize all optimizations at the zero stencil; even from this uninformative start, the energy-constrained learner recovers stencils close to classical centered differences. Figure 3 shows that for $R = 1$ all four solvers achieve comparable accuracy, with errors on the order of 5×10^{-3} . As the radius increases, the behavior diverges: the projected-gradient and Nesterov methods exhibit substantially larger errors, with PG reaching $\mathcal{O}(1)$ error and NAG reaching $\mathcal{O}(10^{-2})$ for $R = 3$. In contrast, the ADMM and CVX solutions maintain errors in a narrow band between approximately 3×10^{-3} and 6×10^{-3} for all radii tested. This indicates that the second-order KKT solve in ADMM and the interior-point method in CVX are more effective at exploiting the additional degrees of freedom introduced by larger stencils, whereas the first-order projected methods struggle to fully optimize the objective within the available iteration budget. We believe the gap for larger R is primarily due to conditioning and the fact that PG/NAG only project onto the equality constraint, whereas ADMM/CVX solve the full KKT system with box constraints. Intersection projections (e.g., Dykstra) could close this gap but would blur the simplicity advantage of PG/NAG; we leave such variants to future work.

6.4 Discrete energy conservation for learned Maxwell stencils

We next examine how closely the learned stencils preserve the semi-discrete electromagnetic energy under Crank–Nicolson time integration.

Figure 4 compares the discrete electromagnetic energy error $\mathcal{E}^n - \mathcal{E}^0$ for Crank–Nicolson time integration using the exact central-difference stencil and the structure-preserving learned stencils. On the linear scale, all curves are essentially flat and remain at the level of 10^{-12} , indicating that the total energy is conserved up to machine precision for all methods. The logarithmic view reveals

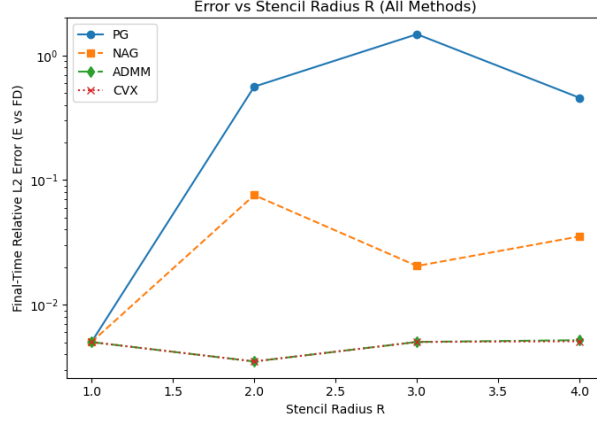


Figure 3: Final-time relative L^2 error in the electric field versus stencil radius R for each solver, using Crank–Nicolson time integration.

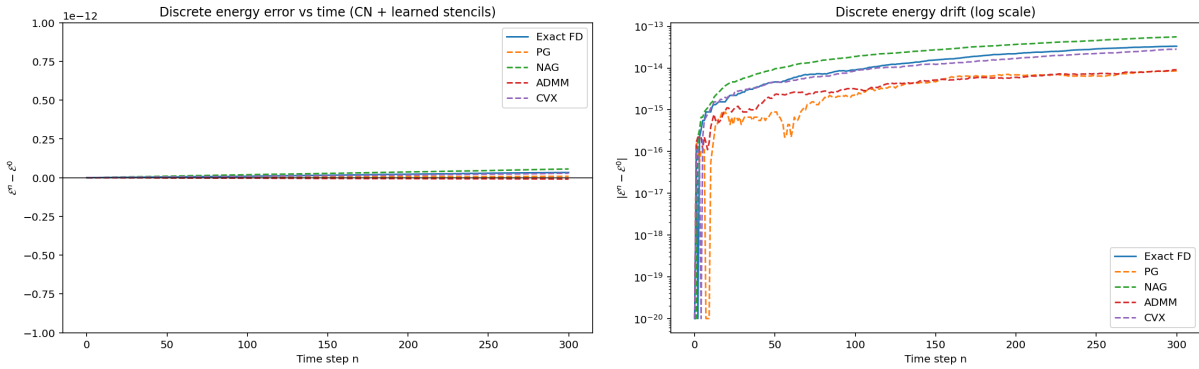


Figure 4: Discrete energy error $\mathcal{E}^n - \mathcal{E}^0$ for Crank–Nicolson time stepping with the exact central-difference stencil and the structure-preserving learned stencils, shown on a linear (left) and logarithmic (right) scale.

small differences: the PG, ADMM, and CVX stencils produce energy drift of the same order as the exact FD stencil, while NAG exhibits a slightly larger but still very small drift. These results confirm that enforcing the skew-symmetry constraints during training yields learned stencils that are effectively energy-preserving under Crank–Nicolson time stepping.

6.5 Dispersion analysis.

To complement the end-time L^2 error metrics, we carry out a Fourier dispersion analysis of the semi-discrete Maxwell system with Crank–Nicolson time stepping. For a given stencil w with Fourier symbol $\lambda(\theta)$, the one-step Crank–Nicolson update for each Fourier mode has eigenvalue

$$\mu(\theta) = \frac{1 + \frac{\Delta t}{2} \lambda(\theta)}{1 - \frac{\Delta t}{2} \lambda(\theta)}.$$

We plot the amplification factor $|\mu(\theta)|$ and the normalized phase $\arg \mu(\theta)/\theta$ as functions of $\theta \in (0, \pi]$, and compare the learned energy-constrained stencils with standard centered-difference stencils of the same radius R ; see Figs. 5a–5b.

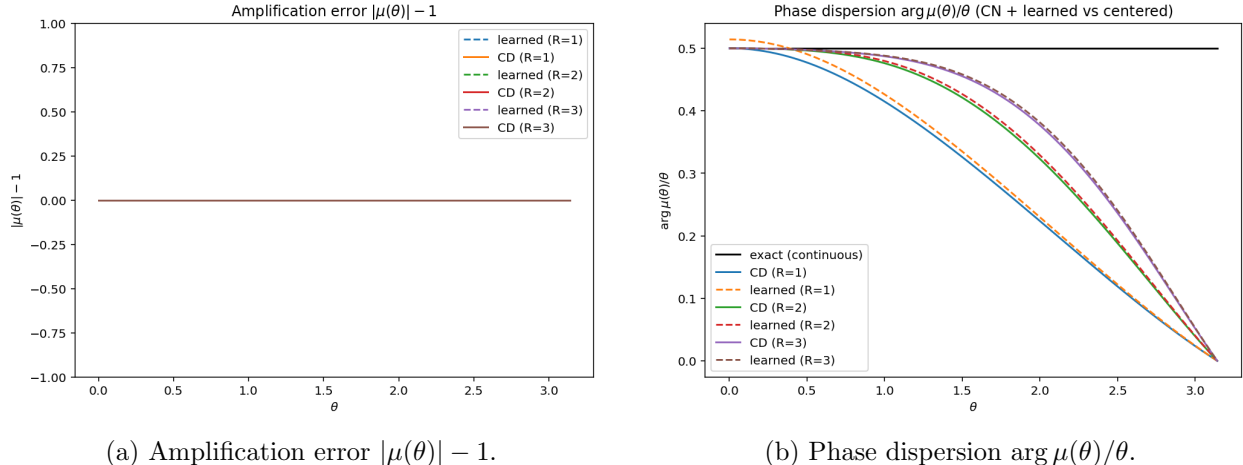


Figure 5: Fourier dispersion analysis of the semi-discrete Maxwell system with Crank–Nicolson time stepping: (a) amplification error and (b) phase dispersion for learned vs. centered-difference stencils.

Figure 5a shows that $|\mu(\theta)| \approx 1$ for all learned stencils and all wavenumbers, essentially indistinguishable from the centered-difference curves and the continuous reference. This confirms that the fully discrete schemes are non-dissipative and preserve the discrete electromagnetic energy in practice, consistent with the skew-adjointness constraints imposed on D .

The phase plots in Fig. 5b provide a more stringent test of accuracy. For $R = 1, 2, 3$, the dispersion curves $\arg \mu(\theta)/\theta$ of the learned operators closely track those of the corresponding centered differences over the range of resolved wavenumbers, with only small deviations at the highest modes; in some mid-frequency bands the learned stencils are slightly closer to the continuous reference. Overall, this mode-by-mode dispersion analysis is more diagnostic than end-time L^2 errors and confirms that the hard skew-adjointness constraints produce learned stencils with physically meaningful wave-propagation properties. see, e.g., [21, 2]

6.6 Learning a nonstandard skew-adjoint operator

To mimic an effective spatial operator arising from unresolved heterogeneity or subgrid physics, we consider a “nonstandard” convolution stencil $w^* \in \mathbb{R}^{2R+1}$ with radius $R = 2$ that is skew-adjoint (i.e., satisfies the constraints (11)) but does not coincide with the usual fourth-order centered difference coefficients. In this setting the analytic form of the differential operator is not available, but we can still generate high-fidelity training trajectories by evolving Maxwell’s equations using w^* .

We then (i) learn an energy-constrained stencil w_{QP} by solving the quadratic program (20) with ADMM, and (ii) compare it to the standard centered-difference stencil w_{CD} of the same radius. Numerically we obtain

$$\frac{\|w_{\text{QP}} - w^*\|_2}{\|w^*\|_2} \approx 6 \times 10^{-8}, \quad \frac{\|w_{\text{CD}} - w^*\|_2}{\|w^*\|_2} \approx 2.5 \times 10^{-1},$$

so the learned operator recovers the nonstandard stencil to nearly machine precision, while the standard stencil incurs a 25% relative coefficient error.

Figure 6a compares the final-time electric field $E(x, T)$ produced by w^* , w_{CD} , and w_{QP} . The centered-difference stencil exhibits a systematic phase and amplitude error, whereas the learned

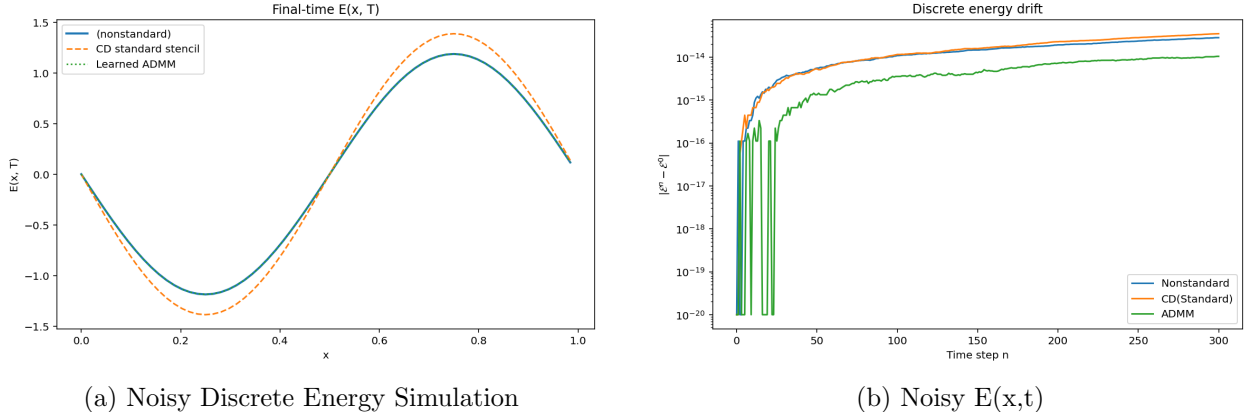


Figure 6: Nonstandard vs Standard Skew-adjoint operator

stencil is indistinguishable from the nonstandard operator. At the same time, all three stencils remain essentially energy-preserving under Crank–Nicolson time stepping (Figure 6b), demonstrating that the proposed method can capture effective, nonstandard differential operators while retaining a discrete Poynting theorem.

6.7 Noisy training and ill-posed least squares

$$\min_{w \in \mathbb{R}^{2R+1}} \frac{1}{2} \|Aw - b\|_2^2 + \frac{\lambda}{2} \|w\|_2^2, \quad (24)$$

To emulate noisy or partially inconsistent experimental data, we add Gaussian noise to the time derivatives dU/dt used in the regression problem (24). Specifically, we draw $d\tilde{U}/dt = dU/dt + \eta$ with η i.i.d. $N(0, \sigma^2)$ and form the corresponding least-squares system (A, b_{noisy}) . We then compute three stencils: (i) the standard centered difference w_{CD} , (ii) an unconstrained least-squares stencil w_{LS} obtained by minimizing (24) with no constraints, and (iii) an energy-constrained stencil w_{QP} obtained by solving the quadratic program (20) with the same noisy data.

Although w_{LS} achieves a very small training error, it violates the skew-adjointness constraints and develops very large high-frequency coefficients. When used in Crank–Nicolson time stepping, the resulting Maxwell semi-discretization is no longer energy-stable, and the discrete energy \mathcal{E}^n blows up (Figure 7a). In contrast, the energy-constrained stencil w_{QP} remains exactly skew-adjoint by construction and yields stable dynamics with energy drift comparable to the hand-derived centered difference stencil.

Figure 7b shows the final-time electric field $E(x, T)$ for all three operators. The solution obtained with w_{QP} is visually indistinguishable from the Central difference baseline, while the unconstrained LS stencil produces a completely corrupted field. This experiment illustrates a regime where training data are noisy or mildly inconsistent, and the energy constraints act as a form of physics-based regularization: they prevent overfitting to noise and guarantee a discrete Poynting theorem irrespective of the data quality.

6.8 Solver convergence and runtime

Finally, we compare the convergence histories of the different solvers. Figure 9a plots the objective value versus iteration for each first-order method for a fixed radius. Figure 9b shows the same objective versus wall-clock time. These plots illustrate the tradeoffs among PG, NAG, and ADMM in terms of iterations, per-iteration cost, and constraint enforcement.

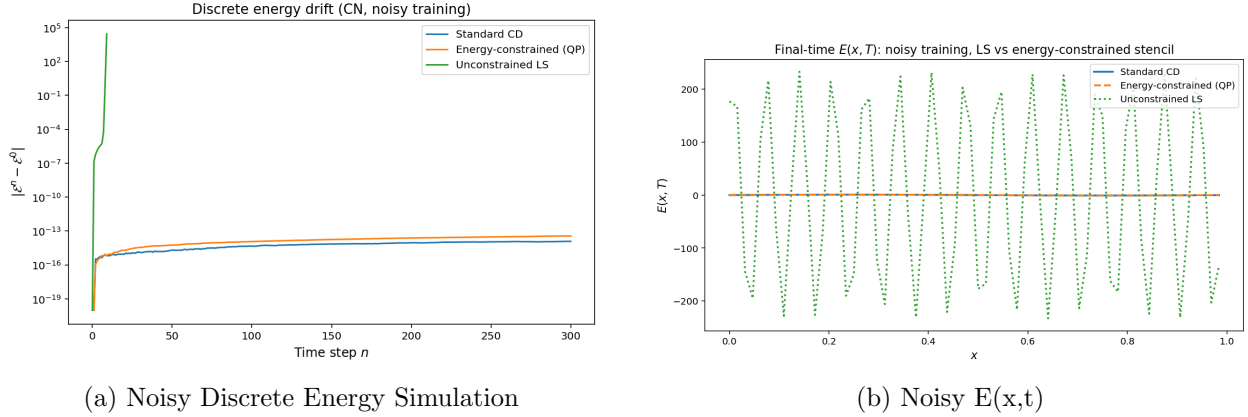


Figure 7: Noisy training and ill-posed least squares

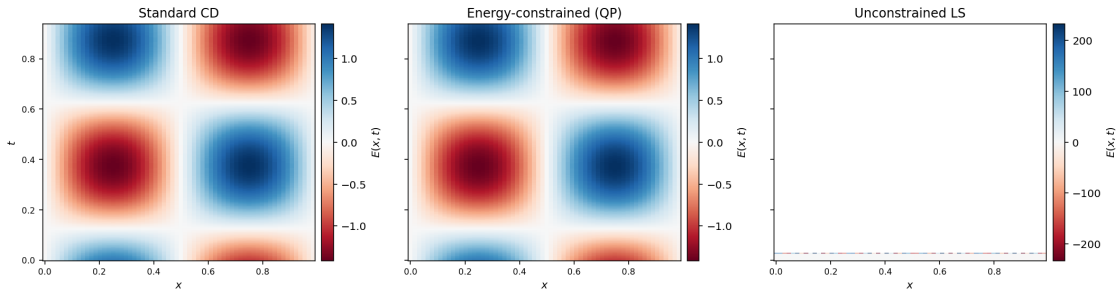


Figure 8: Space-Time Plot of the Electric Field Under Noise Perturbation

Figure 9a shows that all three methods reduce the objective by several orders of magnitude, but their convergence patterns differ. PG exhibits the expected monotone, roughly geometric decrease. NAG achieves a much faster reduction in the first ~ 20 iterations, but with the characteristic oscillations of accelerated gradient methods before settling near the optimum. ADMM appears as an almost flat curve at the bottom of the plot because it solves a small KKT system at each iteration; in this setting, one or two ADMM iterations are enough to reach an objective value comparable to the final PG/NAG iterates.

Figure 9b plots the same objective values against wall-clock time. Because PG and NAG have very cheap iterations, their curves almost coincide and reach a low objective well below 10^{-3} in about 10^{-2} seconds for our problem size. ADMM has a higher per-iteration cost due to the linear solve, but it reaches essentially its final objective in a single step, so the total runtime is competitive with the first-order methods in this regime. For larger-scale problems, we expect the trade-off between cheap but many iterations (PG/NAG) and expensive but very few iterations (ADMM) to be even more pronounced.

7 Conclusion

We proposed an energy-conserving, data-driven discretization framework for the one-dimensional Maxwell system. By learning convolution stencils from spectral training data under a linear skew-symmetry constraint, we obtain discrete derivative operators that are guaranteed to be skew-adjoint and therefore exactly conserve semi-discrete electromagnetic energy. Numerical experiments show that the resulting schemes match the accuracy of standard central differences while preserving

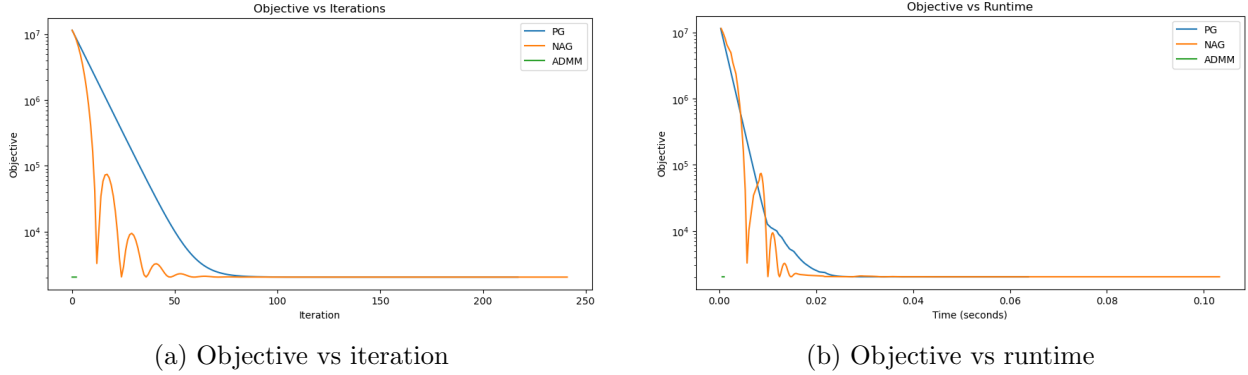


Figure 9: Convergence behavior of PG, NAG, and ADMM for a fixed stencil radius R . Left: objective value versus iteration count. Right: objective value versus wall-clock runtime.

these structural properties. Using Crank–Nicolson time integration, we further confirmed that the discrete energy remains constant to roundoff for learned stencils satisfying the skew-adjoint constraint.

8 Discussion and extensions

Our results show that simple linear constraints can encode key physics in data-driven discretizations: enforcing $Cw = d$ yields skew-adjoint spatial operators that exactly preserve a semi-discrete energy identity, while remaining close to standard centered differences in the homogeneous 1D setting.

To probe more realistic regimes, we also considered (i) a nonstandard target operator whose stencil does not match any classical centered-difference formula and showed that the constrained learner accurately recovers its space–time behavior, while the matching CD stencil incurs noticeable error, and (ii) a noisy regression experiment in which unconstrained least squares produces large coefficients and severe energy drift, whereas the energy- and box-constrained stencil stays well-conditioned, energy-stable, and faithful to the clean baseline $E(x, t)$.

These examples suggest that physics-motivated constraints can regularize noisy or mildly misspecified regression problems and make it feasible to learn effective Maxwell operators in settings where analytic stencils are difficult to derive or tune (e.g., heterogeneous media or band-limited/experimental data). A natural next step is to extend the same constrained-learning philosophy to staggered curl operators on Yee grids in 2D/3D, enforcing block skew-symmetry to preserve a discrete Poynting theorem, and to couple the learned operators with simple dispersive material models and absorbing layers in more realistic FDTD setups.

Acknowledgements

The author gratefully acknowledges Profs. Xiao Fu and Nathan Gibson for valuable guidance and feedback throughout this work.

References

- [1] J. Bar-Sinai, S. Hoyer, J. Hickey, and M. Levine. Learning data-driven discretizations for partial differential equations. *Proceedings of the National Academy of Sciences*, 116(31):15344–

- 15349, 2019.
- [2] Vrushali A. Bokil and Nathan L. Gibson. Analysis of spatial high-order finite difference methods for maxwell’s equations in dispersive media. *IMA Journal of Numerical Analysis*, 31(3):1322–1350, 2011.
 - [3] Vrushali A. Bokil, Olivia A. Keefer, and Amy C.-Y. Leung. Operator splitting methods for maxwell’s equations in dispersive media with orientational polarization. *Journal of Computational and Applied Mathematics*, 263:160–188, 2014.
 - [4] Stephen Boyd, Neal Parikh, Eric Chu, Borja Peleato, and Jonathan Eckstein. Distributed optimization and statistical learning via the alternating direction method of multipliers. *Foundations and Trends in Machine Learning*, 3(1):1–122, 2011.
 - [5] Xiao Fu. Lecture 1: Introduction to classification. Lecture Notes, Oregon State University, 2024. Available from the instructor’s course materials.
 - [6] Ernst Hairer, Christian Lubich, and Gerhard Wanner. *Geometric Numerical Integration: Structure-Preserving Algorithms for Ordinary Differential Equations*. Springer, 2nd edition, 2006.
 - [7] Ernst Hairer and Gerhard Wanner. *Solving Ordinary Differential Equations II: Stiff and Differential-Algebraic Problems*, volume 14 of *Springer Series in Computational Mathematics*. Springer, 2 edition, 2010.
 - [8] Alexander Heinlein, Yuwei Chen, and George E. Karniadakis. Multi-fidelity domain-decomposition physics-informed neural operators for time-dependent partial differential equations. *arXiv preprint arXiv:2508.03774*, 2025.
 - [9] Dmitrii Kochkov, Jamie A. Smith, Ayya Alieva, Qing Wang, Michael P. Brenner, and Stephan Hoyer. Machine learning–accelerated computational fluid dynamics. *Proceedings of the National Academy of Sciences*, 118(21):e2101784118, 2021.
 - [10] Randall J. LeVeque. *Finite Difference Methods for Ordinary and Partial Differential Equations*. SIAM, 2007.
 - [11] Julia Ling, Andrew Kurzawski, and Jeremy Templeton. Reynolds averaged turbulence modelling using deep neural networks with embedded invariance. *Journal of Fluid Mechanics*, 807:155–166, 2016.
 - [12] Cheng Liu, Johannes Brandstetter, Nils Thuerey, and Kiwon Um. clawno: Conservation law–encoded neural operators. *Advances in Neural Information Processing Systems*, 37, 2024.
 - [13] Yuxuan Liu, Harsh Patel, Ana Renganathan, and Lu Lu. Conservation-preserved fourier neural operator through adaptive correction. *Computer Methods in Applied Mechanics and Engineering*, 2025. To appear.
 - [14] Yunfan Ma, Mingfei Wu, Zhihao Peng, Baile Zhang, and Zhenglong Xu. Pic²o-sim: A physics-inspired causality-aware dynamic convolutional neural operator for ultra-fast photonic device fdtd simulation. *arXiv preprint arXiv:2406.17810*, 2024.
 - [15] Yunan Mao, Yiming Li, Luca Magri, and George E. Karniadakis. Towards general neural surrogate solvers with specialized neural accelerators: Domain-decomposition neural operators for large-scale pdes. *arXiv preprint arXiv:2405.02351*, 2024.

- [16] K. W. Morton and D. F. Mayers. *Numerical Solution of Partial Differential Equations: An Introduction*. Cambridge University Press, 1994.
- [17] Eric J. Parish and Karthik Duraisamy. A paradigm for data-driven predictive modeling using field inversion and machine learning. *Journal of Computational Physics*, 305:758–774, 2016.
- [18] Maziar Raissi, Paris Perdikaris, and George E. Karniadakis. Hidden physics models: Machine learning of nonlinear partial differential equations. *Journal of Computational Physics*, 357:125–141, 2018.
- [19] R. D. Richtmyer and K. W. Morton. *Difference Methods for Initial-Value Problems*. Wiley-Interscience, 2 edition, 1967.
- [20] Samuel H. Rudy, Steven L. Brunton, Joshua L. Proctor, and J. Nathan Kutz. Data-driven discovery of partial differential equations. *Science Advances*, 3(4):e1602614, 2017.
- [21] Allen Taflove and Susan C. Hagness. *Computational Electrodynamics: The Finite-Difference Time-Domain Method*. Artech House, 3rd edition, 2005.